

1

2

4

7

8

9

10

1

12

13

Sediment core: sample processing and unsaturated conditions

Fig. S1.1 shows the set-up of the sediment press used to squeeze sediments from the sediment core liners into the copper tubes. A piston (not shown) pushes freshly collected sediments contained in the liner, which is held in place by a cylindrical metal core holder, into a copper tube using a mechanical press. The copper tube is attached by Swagelok connectors. Once the sediments have flushed the copper tube sufficiently, the clamps are sealed, and the copper tube disconnected. Copper tubes are then transported back to Switzerland for further preparation and centrifugation to separate the pore water from the sediment matrix (see Methods).

Upon sample preparation, samples specifically at depths of 8.25, 8.75, 11.75, 12.75, 13.25 and 14.25 m showed features representative of unsaturated conditions. Gas pockets or bubbles were observed (Fig. S1.2) in the sampled sediments at the above-mentioned depths, and while the sediments felt damp, they did not give the appearance to be water saturated. These observations are clearly reflected in the noble gas ratio data of Fig 2., whereby all the aforementioned samples are situated in cluster U.

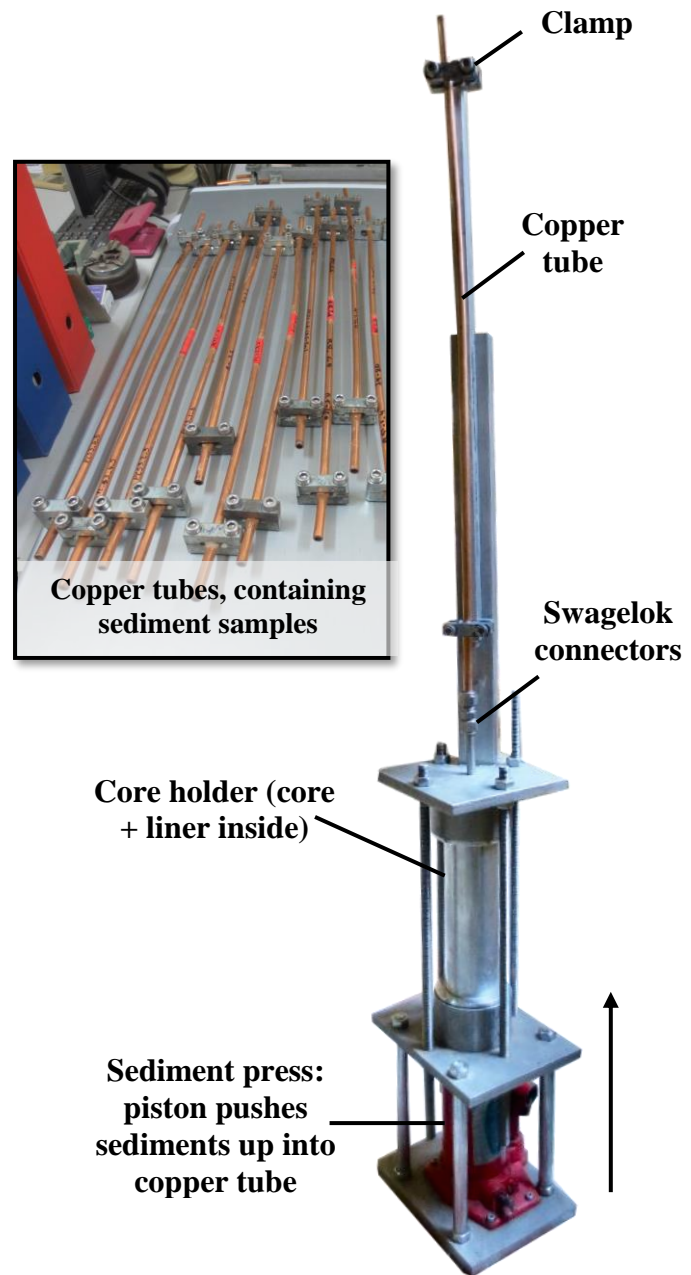


Figure S1.1: Sediment press with attached copper tube. Inset: copper tubes filled with sediments as collected in the field.

Such observations were noted from the discarded pieces of copper tubes containing sediments, during the preparation of cutting the larger 60 cm piece into smaller aliquots, and

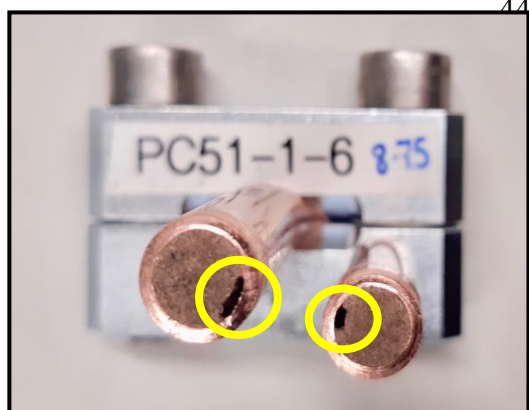


Figure S1.2: Slice through a leftover copper tube sediment sample (including clamp), showing an observable gas bubble in the sediments as circled.

prior to centrifugation. After centrifugation, a similar observation was made. For centrifugation, duplicate samples are routinely opened to find reasonably where the sediment-water interface is, and it is therefore known where to clamp the sample to be analysed such that only a water sample remains (Tomonaga et al., 2011). When opening the duplicate samples for those aliquots in cluster U, however, a sediment-gaseous interface was observed alongside only minute amounts of water or

moisture. It was therefore anticipated prior to analysis, that those samples might show noble gas ratios differing to those expected in ASW (e.g., more air-like).

Increased sand content and conductivity in unsaturated layers

To support the evaluation of saturated and unsaturated layers in the investigated sediment core, we compared our data to known sand content and hydraulic conductivity data for a sediment core taken around 200 m downstream (along the transect; Eiche et al., 2008). The sand percentile and hydraulic conductivity increase in the layers we identify in our aquitard sediment core (located at the village's health clinic) as unsaturated, with a small potential offset of around 1.5 m in the upper layer (Fig. S2). The contrary is also true, in which the layers with a reduced sand content (increasing silt-clay content) and conductivity at depths between 9 - 11.5 m, coincides with a lower $^3\text{He}/^4\text{He}$ ratio, as is expected in more consolidated sediments (see also Fig. 3).

We note that the hydraulic conductivity shows also a relatively smaller increase as compared to the sand content in the upper layer. However, given that we compare our data to a core situated some 200 m away, and that the stratigraphy of the layers in this aquitard are most likely subject to some spatial variation, our results are generally in good agreement with the data from Eiche et al. (2008).

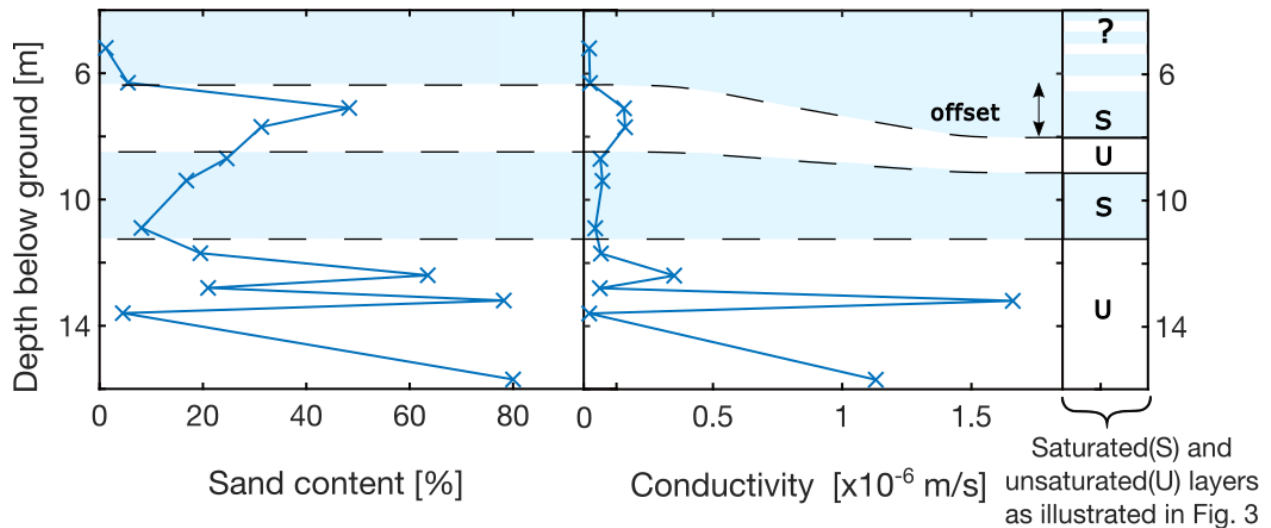


Figure S2: The sand content and hydraulic conductivity vs. depth through the aquitard of a sediment core taken around 200 m downstream from where the sediment core in our study was taken (data adapted from Eiche et al., 2008). The bar on the right indicates the U and S layers as defined from the sediment core in our study (see also Figs. 2, 3) and how these layers might correspond to the sand content and hydraulic conductivity data, showing also a small offset in the upper U layer.

Hydrostatic pressure and CH₄ saturation concentrations: a comparison with previous studies

Calculations from Stopelli et al. (2021) suggest an in-situ CH₄ saturation concentration in zone A of around $6.0 \times 10^{-2} \text{ cm}^3_{\text{STP}}/\text{g}$ (43 mg/L), for a well depth of 20 m and a hydraulic head at 8 m b.g.l (below ground level). In Lightfoot et al. (2022), saturation concentrations of $7.2 \times 10^{-2} \text{ cm}^3_{\text{STP}}/\text{g}$ (52 mg/L) were assumed for a well depth of 23 m and the same head depth, i.e., close to zone B. As previously described (see Results) our study suggests that the height of the overlying water column is anticipated to be reduced by approximately 4 m, leading to a reduced hydrostatic pressure of approximately 30%. Consequentially, the in-situ CH₄ saturation concentration is also lowered to around $5.2 \times 10^{-2} \text{ cm}^3_{\text{STP}}/\text{g}$ (37 mg/L) and is therefore a respective 15% and 30% lower than previous saturation concentrations applied in Stopelli et al. (2021), and Lightfoot et al. (2022). In the above calculations, the equation for the hydrostatic pressure has been applied: $P_{\text{hyd}} = \rho gh$; where ρ is the density of water (997 kg/m^3); g the acceleration due to gravity (9.8 m/s^2); and h (in m) is the height of the water column.

Aquitard pore space: further noble gas analysis

Fig. S3 illustrates a plot of the $^3\text{He}/^4\text{He}$ ratios vs. the Ne/He ratios of the aquitard pore space. A similar clustering of the data is observed as was illustrated with the Ne , Ar and Kr noble gas ratios in Fig. 2, although the clusters are not so distinct given the close proximity of the data points. For the samples situated in the unsaturated cluster (U), the respective $^3\text{He}/^4\text{He}$ ratios are close to, or above the $^3\text{He}/^4\text{He}$ ratio in air and ASW (with the exception of one sample at a depth of 11.75 m). Interestingly, the U cluster samples seem to exhibit a small accumulation

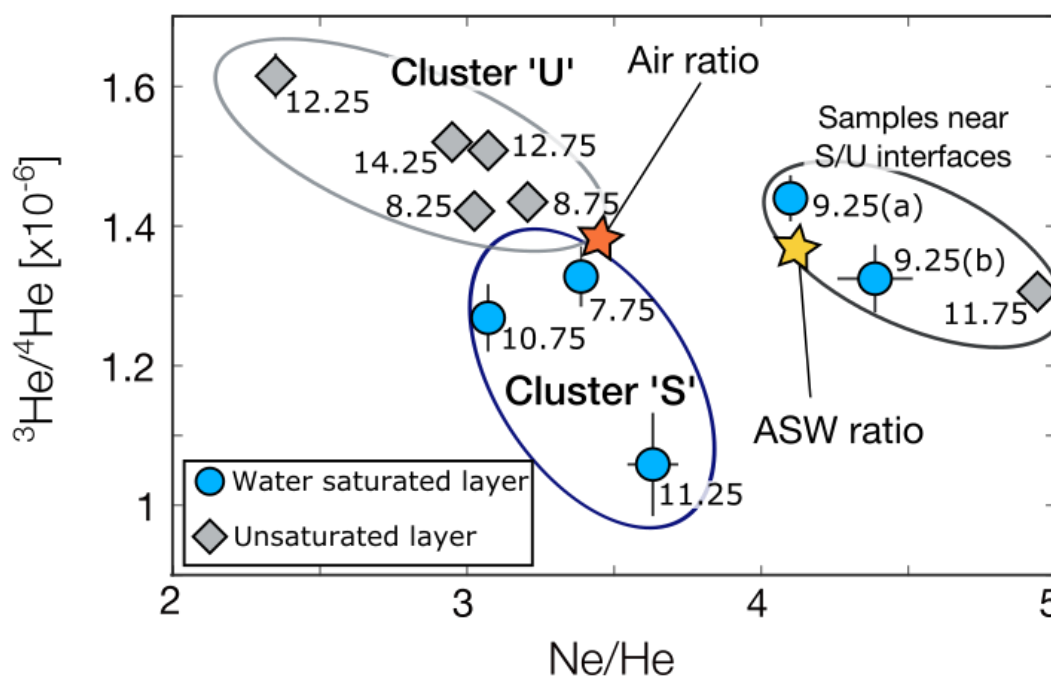


Figure S3: $^3\text{He}/^4\text{He}$ ratio vs. Ne/He ratio of the pore space samples through the aquitard. Numbers indicate sample depths in meters. Some similar groupings (as with the Ne , Ar and Kr ratio data in Fig. 3) between the saturated (S) and unsaturated (U) clusters are observed. While the U samples in general show a slightly higher $^3\text{He}/^4\text{He}$ ratio than air, several of the corresponding Ne/He ratios are actually lower than the air ratio, indicating an ‘aged’-air or gaseous phase.

of radiogenic ^4He , as observed only when considering the Ne/He ratios, which are below the Ne/He ratio of air. As such, the U cluster samples seem to exhibit ‘aged air/gas’ in the unsaturated pore space.

Samples situated in the water saturated cluster (S), generally show both $^3\text{He}/^4\text{He}$ and Ne/He ratios to be lower than the respective ratios in ASW, which confirms accumulation of radiogenic ^4He . A third grouping in this data set has been established for those samples close to a S/U interface. The two samples at a depth of 9.25 m have concentrations close to ASW, as may be expected near the outer most (top) part of a confined layer, where water begins to

108 saturate the pore space, but ^4He has not yet had enough time to accumulate. The following
109 sample in the saturated layer, at a depth of 10.75 m, contains considerably more radiogenic
110 ^4He , thus lowering both the $^3\text{He}/^4\text{He}$ and Ne/He ratios.

111 The sample at depth 11.25 m, close to the lower S/U interface (see Fig. 3), shows a slightly
112 higher Ne/He ratio while the $^3\text{He}/^4\text{He}$ ratio decreases, relative to the above sample at 10.75 m.
113 This observation is somewhat conflicting. However, given the proximity of sample 11.25 (m)
114 to the underlying unsaturated layer, these observations could be explained by hypothesizing
115 that the rate at which He diffuses into the underlying layer (without fractionation of the He
116 isotopes), is greater than the rate of radiogenic accumulation in the saturated layer i.e., implying
117 a net loss of He from the saturated layer. A net loss of He to the lower unsaturated layer, is also
118 supported by the $^3\text{He}/^4\text{He}$ ratio observed in sample at 11.75 m (see also Fig. 3), where the
119 effective $^3\text{He}/^4\text{He}$ ratio is significantly lower than for other samples in the same unsaturated
120 layer, thus indicating ^4He input from the above saturated layer.

121 Collectively, some of the unusual observations in the lighter noble gas ratios at or close to
122 the S/U interfaces, could be attributed to both the potential radiogenic input (of He), and
123 changes in the gas dynamics between the water and gaseous phases at those specific locations
124 within the sediment core. Thus, the exchange of gases between the saturated and unsaturated
125 layers seems necessary to reasonably explain some of the above observations.

126 127 **Groundwater samples: comparison with a previous in-situ analysis**

128
129 Fig. S4 compares the Ar and Kr data in this study, to that from our previous study in
130 Lightfoot et al. (2022), where noble and reactive gases in the groundwater at Van Phuc was
131 analysed in the field with a portable mass spectrometer (also called miniRUEDI; see
132 Brennwald et al., 2016). As the online measurements from the miniRUEDI are highly robust
133 in terms of minimising degassing artefacts on sampling, the aim in comparing data sets is to

elucidate the possibility of degassing upon sampling with the copper tubes, specifically for Ar and Kr.

While there is indeed a slight divergence (as seen in the polynomial fits) between the data set taken with the miniRUEDI and the data from our study, the overall conclusions of Ar and Kr data in groundwater remains clear: atmospheric noble gases are highly depleted in response to CH₄ oversaturation and subsequent gas removal (Lightfoot et al., 2022). We are therefore confident that the arguments presented for in-situ degassing for this aquifer, particularly in terms of Ar and Kr concentrations, are well justified.

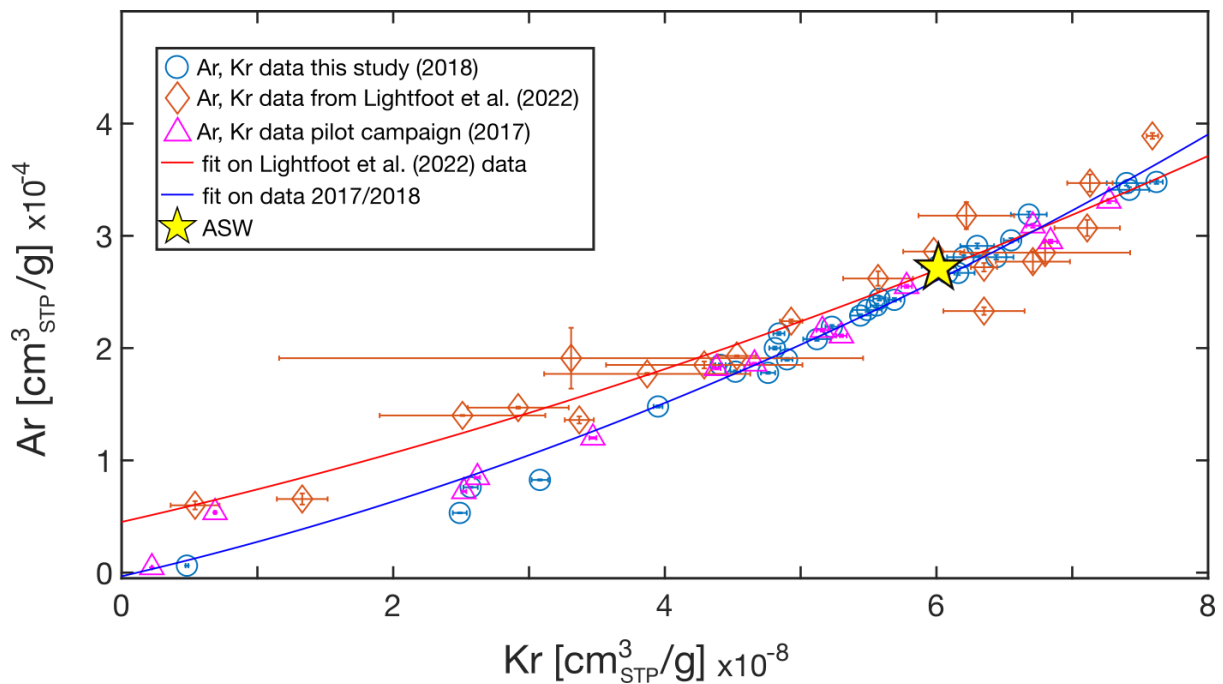


Figure S4: Comparison of Ar and Kr concentrations in groundwater at the study site (as collected in copper tubes; blue circles and pink triangles), with data from a previous study (Lightfoot et al., 2022; red diamonds), which analysed the noble gas concentrations of Ar and Kr directly in the field using a portable mass spectrometer. The year in parenthesis on the data in this study indicates sampling year, whereby some samples in copper tubes were taken from a pilot field campaign carried out in 2017. Air saturated water (ASW) is identified as a yellow star.

Groundwater: degassing trend supported by general noble gas analysis

Overall, the noble gases Ne and Kr follow a similar pattern to Ar in terms of excess and degassing of the noble gas concentrations in the wells relative to ASW concentrations (Table 3). Generally, for the degassed wells, Ne is more strongly depleted than Ar, relative to ASW concentrations, while Kr is slightly less depleted than Ar. This discrepancy from

degassing is anticipated due to the differences in diffusion coefficients for the different noble gas species (i.e., lower diffusion coefficients for heavier gas species).

Unfortunately, Xe concentrations were only obtained for around half of the samples, due to experimental problems during analysis. However, in those samples successfully analysed, Xe concentrations are in general agreement with the noble gas patterns throughout the transect e.g., an excess air component is observed in well 5, while well 3b shows clear signs of depletion relative to ASW concentrations. He concentrations were also measured; however, since the Ne, Ar and Kr data in general offer a more straightforward interpretation of excess air and depletion in response to degassing (as they do not require disentangling of a potentially significant radiogenic component on both ^3He and ^4He isotopes), only those atmospheric noble gas components are here considered.

161 TABLES

Table 1. Concentrations of noble gases in air (in ppm), and in air saturated water (ASW) at the local prevailing conditions: T = 25°C, S = 0.1 g/kg, altitude = 10 masl. Solubility data to calculate ASW for He, Ne and Ar are taken from Weiss (1970, 1971) and for Kr, solubility data from Weiss & Kyser (1978), was applied. For Xe, solubility data is taken from Clever et al. (1979)

Standard concentrations	³ He/ ⁴ He ratio (no units)	He	Ne	Ar	Kr	Xe
Air [ppm]	1.36 x10 ⁻⁶	5.2	18	9340	1.1	0.09
ASW [cm ³ _{STP} /g]	1.38 x10 ⁻⁶	4.34 x10 ⁻⁸	1.75 x10 ⁻⁷	2.75 x10 ⁻⁴	5.96 x10 ⁻⁸	7.89 x10 ⁻⁹

162
163

Table 2.1. Sediment porewater amounts in cm³_{STP}. Amounts as opposed to concentrations are quoted due to an incomplete separation between the sediments and water (or gas) phase upon centrifugation. As a consequence, only noble gas ratios should be applied for data interpretation. Notably, gas amounts are generally higher in the unsaturated layers than in the water saturated layers. The error on each value is given in parenthesis following the obtained result and applied to the least significant digit(s) e.g., 0.65(1) = (0.65 ± 0.01) x10⁻⁷ cm³_{STP}. Over-all, standard 1σ errors for all individual gases are < 3%, while for the ³He/⁴He ratio the error is < 7%. Errors here tend to be higher than for the usual analysis of water samples, namely because of the small amount of gas measured.

Depth [m]	S/U	³ He/ ⁴ He ratio x10 ⁻⁶	He x10 ⁻⁷ cm ³ _{STP}	Ne x10 ⁻⁷ cm ³ _{STP}	Ar x10 ⁻⁴ cm ³ _{STP}	Kr x10 ⁻⁸ cm ³ _{STP}	Xe x10 ⁻⁸ cm ³ _{STP}
7.75	S	1.33(4)	0.65(1)	2.21(2)	1.68(1)	2.96(3)	0.36(7)
8.25	U	1.42(2)	8.08(3)	24.45(20)	12.71(3)	14.13(12)	1.03(2)
8.75	U	1.43(2)	10.47(5)	33.58(27)	18.67(4)	22.29(17)	1.69(2)
9.25(a)	S	1.44(3)	1.09(1)	4.46(4)	6.38(1)	11.99(10)	1.37(3)
9.25(b)	S	1.32(5)	0.75(1)	3.28(8)	5.56(2)	10.80(10)	1.22(2)
10.75	S	1.27(5)	0.41(1)	1.26(1)	1.60(1)	3.09(3)	0.41(1)
11.25	S	1.06(7)	0.15(1)	0.55(1)	1.38(1)	3.41(4)	0.50(1)
11.75	U	1.31(3)	2.73(7)	13.49(11)	8.11(2)	9.79(8)	0.70(1)
12.25	U	1.62(3)	19.38(7)	45.50(36)	23.70(5)	28.11(23)	2.16(3)
12.75	U	1.51(2)	12.85(5)	39.44(32)	20.88(4)	24.33(20)	1.85(3)
14.25	U	1.52(2)	6.90(3)	20.36(16)	11.40(2)	13.61(12)	1.12(2)

Table 2.2. Sediment porewater or pore-gas ratios. Comparing $^{20}\text{Ne}/^{22}\text{Ne}$ ratios to $^3\text{He}/^4\text{He}$ ratios confirm radiogenic and tritogenic components: $^{20}\text{Ne}/^{22}\text{Ne}$ ratios have a maximum deviation from ASW or air values by -3.6% and +2%, respectively, whereas for the $^3\text{He}/^4\text{He}$ ratios, this deviation is -22% and +15%. Such large deviations from ASW and air ratios in the He ratios, confirm the presence of a radiogenic component. Nevertheless, $^{20}\text{Ne}/^{22}\text{Ne}$ ratios do deviate more than might be expected from their air and ASW ratios, which is most likely a result of the rather small initial gas amounts measured (see table 2.1). Ne/Kr, Ar/Kr and Xe/Kr all clearly indicate fractionation change between the S and U layers. Ne/He ratios have the additional influence of radiogenic ^4He , as described in the SI, Fig. S3.

Depth [m]	S/U	$^{20}\text{Ne}/^{22}\text{Ne}$ ratio*	Ne/He	Ne/Kr	Ar/Kr $\times 10^3$	Xe/Kr $\times 10^{-2}$
7.75	S	9.74(4)	3.39(3)	7.46(9)	5.67(5)	12.01(22)
8.25	U	9.98(1)	3.02(3)	17.30(20)	8.99(8)	7.27(16)
8.75	U	9.88(1)	3.21(3)	15.07(17)	8.38(7)	7.60(12)
9.25(a)	S	9.64(4)	4.10(4)	3.72(4)	5.32(5)	11.39(26)
9.25(b)	S	9.77(2)	4.4(12)	3.04(8)	5.15(6)	11.29(21)
10.75	S	9.70(4)	3.07(3)	4.08(5)	5.18(6)	13.32(37)
11.25	S	9.43(10)	3.63(7)	1.62(2)	4.05(4)	14.71(32)
11.75	U	9.78(1)	4.94(4)	13.78(16)	8.28(7)	7.13(11)
12.25	U	9.98(1)	2.35(2)	16.19(18)	8.43(7)	7.67(12)
12.75	U	9.91(1)	3.07(3)	16.21(19)	8.58(7)	7.61(13)
14.25	U	9.89(1)	2.95(3)	14.96(18)	8.38(8)	8.24(18)

* $^{20}\text{Ne}/^{22}\text{Ne}$ ASW = 9.78; in air = 9.80. Other ratios can be determined from Table 1 (also see Figs. 2 and S3).

Table 3. Sampling (well) coordinates are given alongside the original well name and noble gas concentrations in groundwater. Notably, Xe data is missing for some of the samples due to experimental problems during analysis. The error on each value is given in parenthesis following the obtained result and applied to the least significant digit(s) e.g., $6.21(12) = (6.21 \pm 0.12) \times 10^{-8} \text{ cm}_{\text{STP}}^3/\text{g}$. Standard 1σ errors for individual gases are $< 2\%$ for Ar, Ne, Kr and Xe. The error on ^3H measurements is generally $< 15\%$, with a few outliers as discussed in the caption of Fig. 5.

Simplified well name	Original well name	Depth to screen $\pm 1.5 \text{ m}$	Location Lat/Long DMS	Ne $\times 10^{-7}$ $\text{cm}_{\text{STP}}^3/\text{g}$	Ar $\times 10^{-4}$ $\text{cm}_{\text{STP}}^3/\text{g}$	Kr $\times 10^{-8}$ $\text{cm}_{\text{STP}}^3/\text{g}$	Xe $\times 10^{-9}$ $\text{cm}_{\text{STP}}^3/\text{g}$	^3H TU
1	AMS 12	24	20°54'50.9" N 105°54'21.0" E	1.66(3)	2.81(2)	6.21(12)	-	1.34(5)
2a	VP56	20	20°54'57.9" N 105° 54'11.9" E	0.87(1)	2.19(2)	5.23(5)	7.66(9)	1.22(9)
2b	VP57	30	20°54'57.9" N 105° 54'11.9" E	1.20(1)	2.67(2)	6.08(5)	6.53(7)	1.29(4)
2c	VP58	40	20°54'57.9" N 105° 54'11.9" E	1.21(1)	2.44(2)	5.58(5)	7.62(10)	1.18(4)
3a	PC51	20	20°55'04.1" N 105°53'54.3" E	0.18(1)	0.53(1)	2.49(5)	-	1.64(11)
3b	PC52	28	20°55'04.1" N 105°53'54.3" E	0.49(1)	1.48(1)	3.95(3)	5.24(6)	1.16(5)
3c	VP55	40	20°55'04.1" N 105°53'54.3" E	1.13(1)	2.38(2)	5.56(5)	7.78(9)	1.45(8)
4	Family 2	45	20°55'08.6" N 105°53'50.7" E	1.13(2)	2.34(2)	5.49(11)	-	0.93(27)
5	VP59	20	20°55'15.0" N 105°53'46.2" E	1.93(1)	3.48(2)	7.62(5)	10.01(9)	1.07(8)
6	VPNS3	27	20°55'14.9" N 105°53'46.1" E	2.17(3)	3.19(3)	6.68(13)	-	1.08(16)
7a	AMS5	24	20°55'17.4" N 105°53'41.7" E	0.037(1)	0.062(1)	0.48(1)	-	1.09(12)
7b	VPNS5	35	20°55'17.3" N 105°53'41.8" E	2.15(3)	3.47(2)	7.40(15)	-	1.81(12)
8a	AMS11-25	24	20°55'18.4" N 105°53'38.3" E	0.248(4)	0.76(1)	2.57(5)	-	1.43(18)
8b	AMS11-32	33	20°55'18.4" N 105°53'38.3" E	1.38(2)	2.81(2)	6.44(13)	-	1.00(5)
8c	AMS11-47	48	20°55'18.4" N 105°53'38.3" E	1.70(3)	2.91(2)	6.30(12)	-	0.12(14)
9	PC44	38	20°55'18.5" N 105°53'38.2" E	1.83(3)	3.41(2)	7.42(15)	-	0.52(4)
10	AMS31	25	20°55'18.5" N 105°53'38.2" E	0.87(1)	2.08(2)	5.12(10)	-	1.28(11)
11	PC43	28	20°55'18.7" N 105°53'38.2" E	1.14(1)	2.43(2)	5.69(5)	8.04(9)	1.19(4)
12	AMS32	25	20°55'18.9" N 105°53'37.6" E	0.53(3)	1.78(1)	4.76(5)	6.90(7)	1.73(5)
13	AMS36	27	20°55'19.6" N 105°53'37.6" E	1.39(2)	2.76(2)	6.16(12)	-	0.94(21)
14a	AMS4	23	20°55'19.38" N 105°53'36.17" E	1.51(2)	2.73(2)	6.01(12)	-	1.21(19)
14b	VPNS4	38	20°55'18.9" N 105°53'36.7" E	1.77(2)	2.96(2)	6.55(6)	8.69(10)	0.73(45)
15a	VPMLA-22	21	20°55'23.7" N 105°53'31.1" E	1.05(1)	2.29(1)	5.44(8)	-	0.06(15)
15b	VPMLA-37	37	20°55'23.7" N 105°53'31.1" E	0.91(1)	1.85(1)	4.41(4)	6.67(7)	0.02(3)
15c	VPMLA-52	53	20°55'23.7" N 105°53'31.1" E	1.25(1)	2.13(1)	4.84(4)	6.88(8)	0.03(3)
#1	Family 1	45	20°55'08.3" N 105°54'07.6" E	0.71(1)	1.79(1)	4.52(4)	7.25(8)	1.35(19)
#2	AMS15	24	20°55'35.8" N 105°53'51.7" E	0.78(1)	1.90(1)	4.90(4)	7.32(8)	0.13(4)
#3	AMS13	24	20°54'39.4" N 105°53'36.7" E	0.21(1)	0.83(1)	3.08(6)	-	1.10(13)

REFERENCES

- Brennwald, M. S., Schmidt, M., Oser, J., & Kipfer, R. (2016). A Portable and Autonomous Mass Spectrometric System for On-Site Environmental Gas Analysis. *Environmental Science & Technology*, 50(24), 13455–13463. <https://doi.org/10.1021/acs.est.6b03669>
- Clever, H. L. (1979). In A.S. Kertes, (Ed.), *Krypton, Xenon & Radon: Vol. 2*. Pergamon Press.
- Eiche, E., Neumann, T., Berg, M., Weinman, B., van Geen, A., Norra, S., Berner, Z., Trang, P. T. K., Viet, P. H., & Stüben, D. (2008). Geochemical processes underlying a sharp contrast in groundwater arsenic concentrations in a village on the Red River delta, Vietnam. *Applied Geochemistry*, 23(11), 3143–3154. <https://doi.org/10.1016/j.apgeochem.2008.06.023>
- Lightfoot, A. K., Brennwald, M. S., Prommer, H., Stopelli, E., Berg, M., Glodowska, M., Schneider, M., & Kipfer, R. (2022). Noble gas constraints on the fate of arsenic in groundwater. *Water Research*, 214, 118199. <https://doi.org/10.1016/j.watres.2022.118199>
- Stopelli, E., Duyen, V. T., Prommer, H., Glodowska, M., Kappler, A., Schneider, M., Eiche, E., Lightfoot, A. K., Schubert, C. J., Trang, P. K. T., Viet, P. H., Kipfer, R., Winkel, L. H. E., & Berg, M. (2021). Carbon and methane cycling in arsenic-contaminated aquifers. *Water Research*, 200, 117300. <https://doi.org/10.1016/j.watres.2021.117300>
- Tomonaga, Y., Brennwald, M. S., & Kipfer, R. (2011). An improved method for the analysis of dissolved noble gases in the porewater of unconsolidated sediments. *Limnology and Oceanography: Methods*, 9(2), 42–49. <https://doi.org/10.4319/lom.2011.9.42>
- Weiss, R. F. (1970). The solubility of nitrogen, oxygen and argon in water and seawater. *Deep Sea Research and Oceanographic Abstracts*, 17(4), 721–735. [https://doi.org/10.1016/0011-7471\(70\)90037-9](https://doi.org/10.1016/0011-7471(70)90037-9)
- Weiss, R. F. (1971). Solubility of helium and neon in water and seawater. *Journal of Chemical & Engineering Data*, 16(2), 235–241. <https://doi.org/10.1021/je60049a019>

208

209 Weiss, R. F., & Kyser, T. K. (1978). Solubility of krypton in water and sea water. *Journal*

210 *of Chemical & Engineering Data*, 23(1), 69–72. <https://doi.org/10.1021/je60076a014>

211